Computers and Geotechnics 157 (2023) 105331

Contents lists available at ScienceDirect

Computers and Geotechnics

journal homepage: www.elsevier.com/locate/compgeo

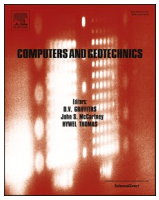

Numerical investigation of the performance of the 3-sided impact roller

Yue Chen [a,*], Mark B. Jaksa [b], Brendan T. Scott [b], Yien-Lik Kuo [b]

[a] School of Engineering and IT, University of New South Wales, Northcott Road, Campbell, Canberra 2612, Australia
[b] School of Civil, Environmental and Mining Engineering, University of Adelaide, SA 5005, Australia

ARTICLE INFO

Keywords:
Rolling dynamic compaction
Impact roller
Ground improvement
Discrete element method

ABSTRACT

Rolling dynamic compaction (RDC) is a soil improvement technique, which involves towing heavy (6–15 t), non-circular (3-, 4-, and 5-sided) modules behind a tractor to achieve soil compaction. Both potential and kinetic energies are imparted to the underlying soil as the modules fall and impact the ground. This paper presents a combined, three-dimensional finite element method (FEM)-discrete element method (DEM) model to investigate the behaviour of the 1:13 scale, 3-sided roller. Numerical results are compared against results from a field study using the corresponding full-size, 3-sided roller in two aspects namely, ground settlements and induced peak pressures. It is demonstrated that the numerical results are in very good agreement with the field observations. This paper examines the influence of the twin modules of the 3-sided roller with respect to ground improvement and the results suggest that the soil beneath a single module is improved solely by the module above it. Therefore, the current practice of using the total weight of the 3-sided roller to predict the energy imparted to the ground and the depth of influence should be avoided. The validated numerical model is also used to predict the energy delivered to the soil and the depth of influence of the roller. The energy imparted to the ground is approximately 22.5 ± 3 kJ per impact with 95% confidence, and the depth of influence is approximately 1.5 m for each of the twin modules of the 13-t, 3-sided roller operating at 11 km/h on granular soils investigated in this study.

1. Introduction

As global population continues to increase unabated, the growing demand for habitation and infrastructure results in construction on sites with poor soil conditions, such as lands with soft, weak and compressible soils. In order to improve soil conditions at such sites, compaction is often adopted as a ground improvement technique, which involves increasing the soil density by means of mechanically applied energies. Air voids within the soil are reduced and soil particles are rearranged during the compaction process. After compaction, the soil has improved shear strength and stiffness, and reduced permeability and settlements (Ranjan and Rao, 2007). In field conditions, compaction is achieved by a number of mechanical techniques, such as drum, sheepsfoot, padfoot, vibrating and impact rollers. Based on the type of applied compactive forces, these techniques are divided into two categories, namely static and dynamic compaction. Static compaction involves densifying soils by applying the self-weight of heavy machinery, while dynamic compaction makes use of repeated high energy impact forces, in addition to the self-weight of the equipment.

This study focuses on rolling dynamic compaction (RDC) which is a dynamic compaction method that has gained its popularity over the past few decades. It involves towing heavy (6–15 t), non-circular modules behind a tractor at relatively constant speed of 10–12 km/h. The modules rotate about their corners and fall to compact the ground. During the compaction process, the soil is densified by the compactive energy, which consists of the potential energy from the self-weight of the modules, the additional potential energy from the modules being lifted about their corners and the kinetic energy derived from the tractor. When compared with the conventional smooth drum roller, RDC is able to improve the ground to a greater depth (1–3 m), since it has a larger module weight and it imparts both potential and kinetic energies simultaneously to the underlying soil. In addition, RDC is towed at a speed range of 10–12 km/h, which is faster than the traditional drum roller speed of 4 km/h (Pinard, 1999). Since RDC is able to compact soil to deeper depths with a relatively faster speed, it has been successfully applied to several large and open ground improvement projects, such as

* Corresponding author.
E-mail addresses: yue.chen4@adfa.edu.au (Y. Chen), mark.jaksa@adelaide.edu.au (M.B. Jaksa), brendan.scott@adelaide.edu.au (B.T. Scott), yien.kuo@adelaide.edu.au (Y.-L. Kuo).

https://doi.org/10.1016/j.compgeo.2023.105331
Received 30 September 2022; Received in revised form 10 February 2023; Accepted 12 February 2023
Available online 23 February 2023

general civil construction works, airports and land reclamation projects, and in the agricultural and mining sectors (Avalle and Grounds, 2004; Davies et al., 2004; Avalle and Mckenzie, 2005; Bouazza and Avalle, 2006).

To date, three different module shape designs of RDC (3, 4 and 5 sides) have been successfully implemented worldwide, with two companies, Broons Pty Ltd., which manufactures and operates the 4-sided module, and Landpac Technologies Pty Ltd., which operates the 3- and 5-sided modules. Fig. 1 presents the three different RDC module shapes. The effectiveness of the 4-sided roller module has been assessed by several researchers by means of field tests (Avalle et al., 2005; Jaksa et al., 2012; Scott and Jaksa, 2015; Scott et al., 2016; Scott et al., 2019b), experimental scale model tests (Rajarathnam et al., 2016; Chung et al., 2017; Chen et al., 2021a), numerical modelling (Kuo et al., 2013; Bradley et al., 2019; Chen et al., 2021b) and machine learning (Ranasinghe et al., 2017a; Ranasinghe et al., 2017b; Ranasinghe et al., 2019). The energy delivered to the soil, the depth of influence, soil settlements, the internal soil movement and the influence of the number of passes and operating speed have been investigated and reported for the 4-sided roller.

When compared with the large volume of research that has been conducted on the 4-sided roller, the efficacy of the 3- and 5-sided rollers has not been extensively studied; at least not in the publicly available literature. Kim (2011) investigated the influence of module shape from three aspects, namely the stress distribution, surface settlements and depth of influence, using the finite element method (FEM) within the LS-DYNA computer program. He reported that the contact area between the roller module and the soil has a great effect on the depth of influence. The limitation of his study was that the adopted soil model and the obtained results were not validated against field data. Bian et al. (2002) developed a numerical model of the 3-sided roller using FEM within NASTRAN. The model was validated by comparing the numerical soil deformation against that calculated theoretically, and the model was then used to investigate the effects of two different module shapes, namely the modules A and B (as shown in Fig. 2), of the 3-sided roller. They concluded that, although the weight, dimensions, and operating speed of these two modules are similar, the slight differences in the slope of the modules' profiles result in different ground improvement outcomes. Module A (solid line in Fig. 2) achieves greater ground settlements when compared with those induced by Module B (dashed line in Fig. 2). Similar to Kim (2011), the key limitation of their study was that the numerical results were not verified using field test results, and hence, the numerical model may not provide reliable predictions of ground improvement due to RDC.

Experimental tests were performed using 1:20 and 1:10 scale models of the 3-sided roller by Rajarathnam et al. (2016) and Li et al. (2020), respectively. The effective depth of influence, particle movements beneath the roller and the effects of operating speed on soil displacements were investigated in their studies. Limitations of their studies were, firstly, the 3-sided roller model was stated not to be a scaled version of any commercial compactors, and therefore, the results of their experimental tests may not be representative of the 3-sided roller used in practice, since even slight differences in the slope of the modules' profile affect the ground improvement outcomes, as stated by Chuanli et al. (2002). Secondly, the distance between the twin modules of the 3-sided roller (as shown in Fig. 1a) was not scaled in accordance with the prototype, and hence, the influence of the twin modules on ground improvement is still unknown. Thirdly, the results of the experimental scale model tests were not compared with or validated against field results.

Previous research has provided a basic understanding of the effectiveness of the 3-sided roller, in order to promote the use of the roller, hence, there is a need to develop a reliable model to provide a better understanding of the ground improvement derived from the roller and to facilitate objective comparison with other module shapes adopted in practice. This paper aims, firstly, to develop a numerical model to simulate the behaviour of the 1:13 scale, Landpac standard 3-sided roller. Ground improvement results obtained from the numerical model are compared against data measured in the field study using the corresponding full-size, 3-sided roller. Secondly, the effectiveness of the 3-sided roller, such as energy delivered to the ground, the depth of

Fig. 1. Different module designs: (a) 3-sided (Landpac), (b) 4-sided (Broons), (c) 5-sided (Landpac).

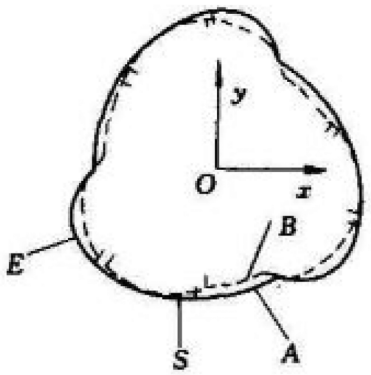

Fig. 2. Two different module shapes examined by (Chuanli et al., 2002).

influence and the influence of the twin modules on ground improvement, as a consequence of the 3-sided roller, are investigated using the validated numerical model.

2. Field tests

Scott conducted a series of field tests to investigate the performance of the full-size, 3-sided roller and surface settlements, pressures induced by the roller and soil densities before and after compaction were provided and confirmed by his email (B.T. Scott, personal communication, 12 August 2021). This field trial was undertaken using a Landpac standard 13-t, 3-sided roller at Monarto Quarries, Callington, South Australia. The 3-sided roller consists of two 6.5-t modules, with each module being 2167 mm high × 900 mm wide. The distance between the two modules is approximately 1170 mm. Due to the distance between the two modules, during compaction, the 3-sided roller leaves an uncompacted region underneath the central frame, i.e. between the two modules. To overcome this, as illustrated in Fig. 3, the 3-sided roller is operated for a second run (displayed in orange, and referred to in practice as a straddling pass) and the roller is translated approximately 1035 mm laterally from the location of the first run (shown in blue). Therefore, for the 3-sided roller, two roller runs is defined as a single roller pass. The depth and length of the trial pad were 1500 and 4000 mm, respectively, and the trial pad was constructed using a homogeneous rock quarry material, which was classified as a well-graded Sandy Gravel, in accordance with the Unified Soil Classification System. The field particle size distribution is presented in Fig. 4. Several in-situ tests were adopted in this field trial before and after compaction, such as field density tests using a nuclear density gauge, dynamic cone penetration tests and the spectral analysis of surface waves (SASW) testing. Surface settlement was also measured between passes to obtain the relationship between the average ground settlement and the number of passes. In addition, as shown in Fig. 3, two Geokon 3400 earth pressure cells (EPCs) were placed beneath the centreline of one of the 3-sided roller modules to measure the pressures induced by the roller. EPCs were buried at depths of 0.7 and 1.1 m below the ground surface. The space between these two EPCs was 1500 mm to avoid stress shadowing due to the bulbous distribution of the vertical pressures induced by the roller. A bespoke accelerometer was attached to each EPC in the *Z*-plane to measure vertical acceleration within the soil as a consequence of the roller. Both the EPCs and the accelerometers were connected to a bespoke data acquisition system and Labview software program (National Instruments, 2019). For every odd run, both the EPCs and accelerometers recorded the pressures and accelerations, respectively, as one of the roller modules passed directly above them, and the roller modules straddled the EPCs and accelerometers with every even run. A total of 80 passes was conducted in this field trial, which consisted of 80 runs of one of the roller modules passing directly over the EPCs, and 80 runs of the roller modules straddling the EPCs, whilst the operating speed of the roller was maintained at 11 km/h.

3. Numerical modelling approach

3.1. Contact model

The commercial software LS-DYNA (LSTC, 2018) is employed to simulate the compaction process in the field trial. The soil is simulated using the discrete element method (DEM) implemented within LS-DYNA, based on the model developed by Cundall and Strack (1979). According to Cundall and Strack (1979), soil particles are modelled as rigid spheres, with soft contacts and the contact forces between particles described using a linear contact model based on a force-displacement law. The motion of each particle is then determined at each time step using Newton's second law of motion according to any unbalanced forces. The linear contact model consists of a linear spring and a viscous dashpot in the normal direction of the contact, a linear spring and a viscous dashpot in the shear direction of the contact, and a frictional slip in the shear direction, with a coefficient of friction (μ). Therefore, the contact forces between particles are composed of linear and dashpot forces. The linear forces are provided by linear springs with constant normal and shear stiffnesses, k_n and k_s, respectively. The dashpot forces are governed by viscous dashpots with normal and shear damping ratios, β_n and β_s, respectively.

The input parameters of the linear contact model are determined from a calibration approach, which involves varying the input parameters until the results of the simulated standard geotechnical tests are consistent with those measured from physical tests. Since, in this study, the numerical results are compared against the field measurements from Scott (B.T. Scott, personal communication, 12 August 2021), the soil used in the numerical model should be consistent with that of the field trial. The soil adopted in the 3-sided roller field tests is the same as that used by Chen et al. (2021b), therefore, the same numerical particle size range and DEM input parameters calibrated by Chen et al. (2021b) are used here. The numerical particle size distribution is included in Fig. 4 and is selected considering the total number of particles, the time step of the numerical model and the dimensions of the roller module (Chen et al., 2021b). In addition, similar to Chen et al. (2021b), the rotation of the spheres is prohibited to mimic the effect of the non-spherical particle shapes used in the field trial. This method helps achieve the realistic macroscopic shear strength of the particle assembly without changing the shape of particles (Calvetti et al., 2003; Calvetti et al., 2004; Gabrieli et al., 2009).

3.2. Simulation of the 3-sided roller

In the numerical simulations, soil particles are modelled using the

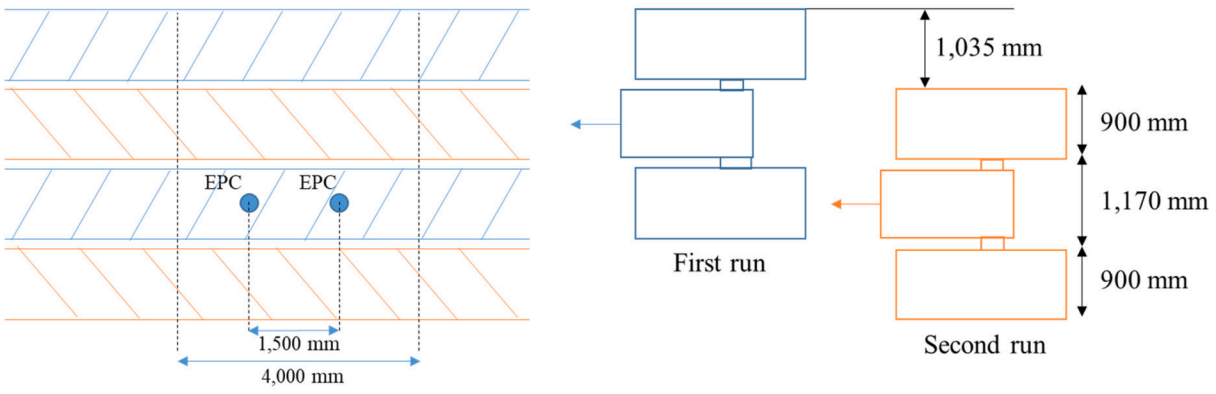

Fig. 3. Field operation of the 3-sided roller.

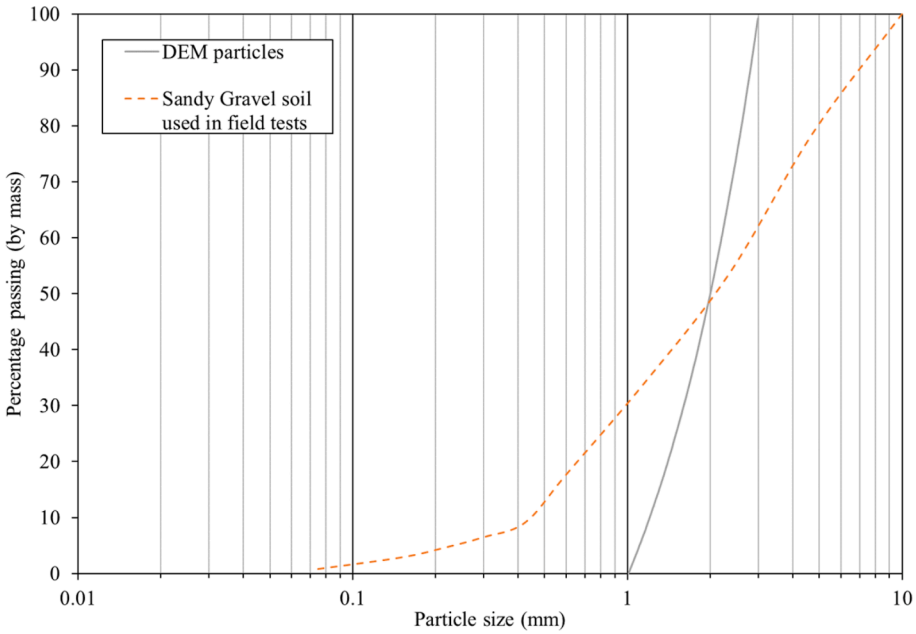

Fig. 4. Particle size distribution curves.

DEM and the 3-sided roller modules are modelled using the FEM, as explained later. Therefore, this numerical model is a combined three-dimensional FEM-DEM model. In LS-DYNA, the contact between finite elements and between discrete and finite elements are handled by a penalty-based contact algorithm. The contact is defined when a finite element node or discrete particle penetrates the contact surface of the finite elements. The contact is treated by placing springs between the contact elements and, hence, the contact force is proportional to the penetration depth and the stiffnesses of these springs. If sliding occurs between the contacts, the contact frictional force is calculated using Coulomb's law of friction.

As shown in Fig. 5, the numerical 3-sided roller model consists of a simplified roller model with two modules, a chamber filled with soil particles, and two rigid bases at each end of the chamber to facilitate the roller's motion. Both the chamber and the two rigid bases are modelled using the FEM as rigid materials without displacement or deformation during the simulation. The size of the chamber is selected as 600 × 400 × 125 mm (length × width × height), giving due consideration to the

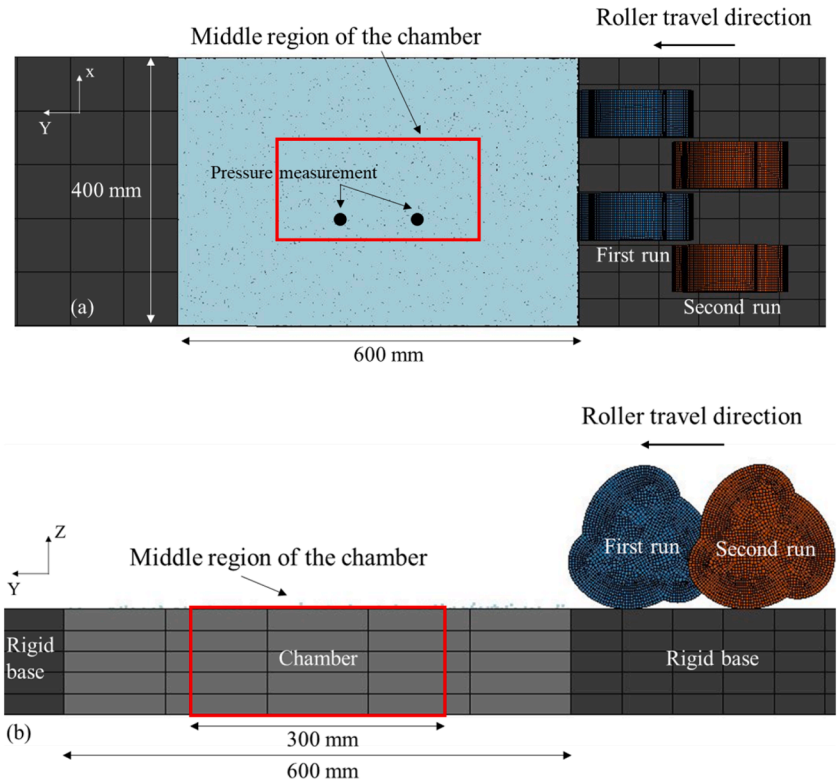

Fig. 5. Setup of the numerical RDC model: (a) plan view, (b) side view.

total number of particles in the numerical model, and hence, computational efficiency, and simulation accuracy. The width of the chamber is sufficient to incorporate the second run (i.e. straddling pass) in a single roller pass. To minimise boundary effects, ground improvement is assessed solely within the middle region of the chamber as shown in Fig. 5.

The roller modules adopted in the simulation are the simplified 1:13 scaled, Landpac standard 13-t, 3-sided roller modules. The tractor in front of the modules, as shown in Fig. 1a, is not included in the simulation since ground improvement caused by the tractor is significantly less than that induced by the roller modules and can be neglected. The 1:13 scaled modules, rather than the full-size modules, are modelled due to computational and time constraints, and is consistent with Chen et al. (2021b). A larger soil area is required in order to simulate the full-size roller modules, which results in a greater number of soil particles in the model. This will then significantly increase the simulation running time. The roller modules are simulated using the FEM as rigid bodies (a rigid material model, *MAT_020 is adopted) with no deformation during the compaction process since the modules are effectively rigid relative to the underlying soil, and this also reduces the simulation time. The Young's modulus of elasticity and Poisson's ratio of the modules are two required input parameters in the model, which are 210 GPa and 0.28, respectively. As illustrated in Fig. 5, two rollers are operated in sequence, as the first and second runs of a single pass in the numerical model, consistent with that in the field trial. The friction coefficient between the soil particles and the roller module is 0.57, which is obtained from the numerical inclined plane test (Chou et al., 2012; Coetzee, 2016).

In the numerical 3-sided roller model, soil particles are generated randomly according to the numerical particle size distribution to fill an enclosed box, and then fall into the chamber under gravity. A rigid plate is placed above the particles and is moved up and down by 20 mm at 200 mm/s for 2 s to compact the particles to help the particles settle in the chamber. The rigid plate is then removed and the RDC process commences after the particles have reached equilibrium. If the particle size range of 1–3 mm is still adopted in the numerical 3-sided roller model, a total number of more than 3.7×10^6 particles will be required, which is beyond current computational abilities and practical simulation running times. It is noted that all simulations were conducted on a supercomputer (2 × Intel Xeon Gold 6248 Processor @ 2.4 GHz) using the ANSYS (LS-DYNA) software and 12 CPU cores. To obtain a manageable number of particles, they are scaled up by a scaling factor of 3.5, which then yields approximately 76,000 particles in the model with a size range of 3.5–10.5 mm. This is consistent with previous simulations by Chen et al. (2021b). The initial soil void ratio in the numerical model is 0.74. According to Ciantia et al. (2015), the D_{50} of scaled particles should be at least one order of magnitude less than the relevant dimension of the model. In this study, the width of the roller module determines the upper limit of particle scaling, since the length of the roller in contact with the soil particles varies while the width of the contact is kept constant when the modules rotate on the ground. The D_{50} of the scaled particles (7 mm) is one order of magnitude lower than the width of the module (69.2 mm, which is treated in greater detail in the following section), which ensures a sufficient number of particles remain in the model after scaling and avoids size effects. The macroscopic response of the particle assembly is maintained by scaling up the calibrated DEM input parameters accordingly (Feng and Owen, 2014; Ciantia et al., 2015). A mass scaling (particle density remains constant before and after scaling) is applied in this study. This scaling law has been successfully employed in many studies to replicate the behaviour of particle assemblies, such as Gabrieli et al. (2009), Evans and Valdes (2011), Ciantia et al. (2016), Chen et al. (2018), Wang et al. (2018) and Zhang et al. (2019). According to the mass scaling law, Young's modulus, the ratio between the shear and normal stiffnesses, the friction coefficient and damping ratios are scale invariant. The normal stiffness depends on the particle scaling factor and has a linear relationship with respect to particle diameter (Gabrieli et al., 2009; Feng and Owen, 2014). Hence, the value of normal stiffness is scaled up by a factor of 3.5 to equal 2.275×10^6 N/m. The upscaled DEM input parameters are included in Chen et al. (2021b).

3.3. Scaling laws

As mentioned above, the full-size, 3-sided roller was adopted in the field trial and a 1:13 scale, 3-sided roller is simulated in the numerical model. In order to compare the numerical scale model results with those obtained from field tests, the standard scaling laws [Eqs. (1)–(6)] developed by Altaee and Fellenius (1994) are used to upscale the numerical results. These scaling laws have been successfully adopted to upscale the results of physical, 1:13 4-sided roller tests by Chung et al. (2017) and to upscale the results of a numerical, 1:13 4-sided roller model by Chen et al. (2021b). Under 1-*g* conditions, the soil has different behaviour at full-scale than at small-scale, as the stress levels at the latter are much lower than those at the former. To achieve constitutive similarity between the full-scale and small-scale models, as proposed by Altaee and Fellenius (1994), the initial soil void ratios in both models should have equal proximity to the steady state line. The slope of the steady state line, $\lambda = 0.11$, is adopted from Chung et al. (2017), since they employed the same soil as that adopted in the field test and in this study. The geometric scaling ratio, *n*, of 1/13 is used in this study. The average initial void ratio of the soil in the field tests was approximately 0.46. Considering a static case when the roller at rest on the ground, in both the field trial and the 1:13 scale model, the ratio of the scale model stress and prototype stress, at the homologous points within the soil, is approximately equal to the geometric scaling ratio (*n*) since the stress is mainly induced by the roller weight. Therefore, the numerical soil initial void ratio of 0.74 is calculated based on the gradient of the steady state line, the field soil initial void ratio, and the stresses in both the field trial and the numerical model. After the DEM particle initialisation, the adopted soil initial void ratio in the numerical model is approximately 0.74, which accords well with that calculated from the scaling law. The same approach to determine the soil initial void ratio in the 1-*g* scale model tests has been adopted in several studies (e.g. Zheng et al., 2017; Lin et al., 2018; Zheng et al., 2020) and they have demonstrated that the performance of soil in 1-*g* scale model tests are representative of the behaviour of the corresponding soil condition in prototype tests using this approach.

$$\frac{L_m}{L_p} = n \tag{1}$$

$$\frac{M_m}{M_p} = n^3 \tag{2}$$

$$\frac{V_m}{V_p} = n \tag{3}$$

$$\frac{D_m}{D_p} = n \bullet \frac{\frac{\Delta e_m}{1+e_{0m}}}{\frac{\Delta e_p}{1+e_{0p}}} \tag{4}$$

$$\frac{\sigma_m}{\sigma_p} = exp\left(\frac{e_{0p} - e_{0m}}{\lambda}\right) \tag{5}$$

$$\frac{E_m}{E_p} = exp\left(\frac{e_{0p} - e_{0m}}{\lambda}\right) \times n^3 \tag{6}$$

where *L* is the characteristic length; *M* is the mass of the roller module; *V* represents the operating speed; *D* is soil vertical displacement; σ is the imposed stress in the soil; *E* is the energy imparted by the roller module; *n* is the geometric scale ratio; e_0 is the initial void ratio; Δe is the change in void ratio; λ is the slope of the steady state line in the $e - \log \sigma$ plane; and the subscripts *m* and *p* denote the scale model and prototype (full-

size roller module in this context), respectively.

The properties (such as, dimensions, weight and operating speed) of the 1:13 3-sided roller are converted from the full-size roller using Eqs. (1)–(3). Hence, the dimensions of the 1:13 3-sided roller module are 166.7 × 69.2 mm (height × width) and the space between the two modules is approximately 90 mm. The weight of each module is 6.5-t in the prototype, therefore, the weight of each module is 2.96 kg for the 1:13 scale model. As mentioned above, in the field study, the full-sized roller travelled at 11 km/h, which corresponds to the 1:13 scale roller operating at a speed of 235 mm/s. Also as mentioned previously, two EPCs were placed beneath the centreline of one of the roller modules, at 0.7 and 1.1 m depths below the ground, to measure pressures in the field trial. Consistent with this, pressures are measured beneath one of the roller modules (as displayed in Fig. 5a) at 55 and 85 mm depths in the numerical model. The numerical 3-sided roller is operated up to 15 passes, which consists of 15 runs of one of the roller modules directly passed over and 15 runs of the roller modules straddled pressure measurements. Using the computing resources mentioned previously, this equates to a total run time of 45 days.

4. Comparisons between numerical model and field trial

Results of the numerical model are compared against those measured in the field tests conducted by Scott (B.T. Scott, personal communication, 12 August 2021). The numerical results are compared against the field measurements from two aspects, namely, ground settlements and pressures at 0.7 and 1.1 m depths. These are each presented in turn.

4.1. Ground settlements

Soil displacement is often used in practice as a direct measurement of ground improvement induced by the roller. In the field trial, ground settlements were measured by surveying using an automatic level and staff. Each settlement reading was obtained from several points on the ground along the roller traverse lane, and then averaged to obtain the average ground settlement. Settlement was measured after every 2 roller passes until pass ten, and then every 5 passes thereafter. In the numerical model, ground settlement induced by the 3-sided roller is obtained from the particle coordinates. The coordinates of an approximately one-particle thick layer of numerical particles, which is located at the ground surface, within the middle region of the chamber, are tracked and averaged after every roller pass. Numerical ground settlements are upscaled to the full scale using Eq. (4), based on the average soil initial void ratios, and the changes in void ratios after 15 passes in the field tests and in the numerical model. The numerical soil void ratios before and after 15 passes are 0.74 and 0.66, respectively. As mentioned above, the average soil initial void ratio in the field study was 0.46. The soil average void ratio after 15 roller passes was approximately 0.42, which is inferred from ground settlements after 15 and 80 passes and the change in void ratio after 80 passes, since the void ratio was only measured before and after the entire 80 passes were completed in the field study.

Fig. 6 presents the upscaled numerical and field ground settlements with respect to the number of passes. In general, as one would expect, ground settlement increases with the increasing number of passes for both the numerical model and field tests. It can be seen that numerical settlement results are in good agreement with those measured in the field. Two trend lines fitted through the numerical and field results have similar shape, which indicates that the numerical model predicts ground settlements induced by the 3-sided roller very well. After 15 passes, the ground settlements indicated by the numerical model and measured in the field trial were 33.8 and 36.5 mm, respectively, which represents a modest difference of 2.7 mm (7.3%). There are a number of possible reasons for this discrepancy. Firstly, in the field tests, as mentioned above, ground settlements were measured by the surveying method. The undulating surface left by the roller may result in inconsistent

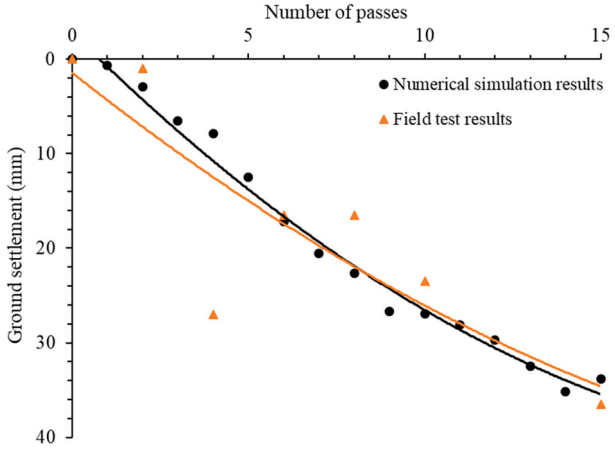

Fig. 6. Ground settlement with respect to the number of passes obtained by the numerical model compared with the field study.

measurements, especially during the first a few passes, e.g. settlement measured at pass 2, as the soil was relatively loose, which is more easily disturbed by the roller. Secondly, the simplified spherical particles adopted in the numerical model are different to the angular sandy gravel soil used in the field. Finally, as shown in Fig. 1a, the nature of the full-size, 3-sided roller is more complex than the simplified numerical model. For example, two wheels are installed between twin modules of the full-size, 3-sided roller to assist in the smooth operation of the roller. Nevertheless, the difference between the numerical and field ground settlements is modest and, it can be concluded that the numerical model is able to, with an appropriate degree of confidence, predict ground settlements as a consequence of the 3-sided roller.

4.2. Peak pressures

The dynamic effects of RDC on the underlying soil can be examined through pressure measurements at different depths of interest. In the field tests, pressures imparted to the soil due to the roller were measured by EPCs. As shown in Fig. 3 and as mentioned previously, two EPCs with a diameter of 230 mm were placed along the centreline of one of the roller module traverse lanes, at 0.7 and 1.1 m depths below the ground. Therefore, the field pressures are the averaged pressures experienced by several soil particles in contact with the EPCs. The diameter of 230 mm equates to 17.7 mm at 1:13 scale model [Eq. (1)], and the D_{50} of the upscaled particles is 7 mm. Therefore, as shown in Fig. 5a, numerical pressures are measured and averaged over two sets of three adjacent particles, within the middle region of the chamber, at 55 and 85 mm depths, respectively. It is worth noting that, according to Davidson et al. (2015), in the DEM model, pressures are determined by the resultant force of that particle, and the resultant force is calculated from the contact force and any externally applied force on that particle. In this study, a single particle always interacts with three to five adjacent particles. Therefore, the numerical pressures are calculated from the contact forces between up to 15 particles. In addition, as mentioned above, pressures were measured by EPCs in the field tests, and each EPC was placed at a single location within the entire trial pad. With each impact, the roller may land in the same or a different location on the ground and hence, it is not possible to capture the maximum pressure as a consequence of the roller for every impact. To account for the effects of non-direct impacts in the field, the distance between the centre of the module face and the centre of the EPC was measured, which is defined as the *offset distance*. In order to simulate this phenomenon, the initial starting location of the roller was varied, and the offset distance is also measured in the numerical model. Therefore, numerical particles used to determine average pressures should be limited to a relatively small number to ensure accuracy of the offset distance measurements.

In the following section, pressures obtained from odd and even runs refer to pressures induced by the roller modules directly over and straddling the location of the pressure measurement (EPCs in field tests), respectively. The numerical peak pressures are upscaled using Eq. (5) based on the initial soil void ratio near 0.7 and 1.1 m depths. In the field trial, the initial void ratio varied with depth and the initial void ratios near 0.7 and 1.1 m depths were 0.45 and 0.47, respectively. Figs. 7 and 8 present the numerical and field peak pressures from the odd and even runs, respectively. It can be seen that peak pressures measured from the odd runs are significantly greater than those obtained from the even runs, as one would expect. The measured peak pressure varies for each run due to the effects of non-direct impacts, and the offset distance is different for each run in the numerical model and the field tests. Therefore, it is difficult to obtain any meaningful relationship between the measured peak pressures and the number of runs, and it is not possible to directly compare the numerical peak pressures with those recorded from the field trial.

In Fig. 9, the numerical and field peak pressures measured from the odd runs are plotted with respect to the offset distance, to investigate the relationship between peak pressure and offset distance. Pressures measured from the even runs are not plotted since, in these runs, the roller module straddles the measurement location, which also has an offset in the lateral direction. The variation of offset distance shows that the roller lands in a different location on the ground at each impact. A wider spread of offset distance was recorded in the field. This may be attributed to the variation of the roller landing location in the field tests being greater than that in the numerical model, which then results in a greater variation in offset distance. Nevertheless, the numerical peak pressure versus offset distance plots display similar trends to those of the field results at both 0.7 and 1.1 m depths. It is obvious that offset distance has a significant influence on the magnitude of peak pressure, and when Fig. 9a is compared with 9b, the effects of offset distance on the pressure readings decrease with depth. This finding is consistent with that reported by Li et al. (2020) and Scott et al. (2020), who stated that the pressure imparted to the soil by the roller dissipates in all directions, i.e. pressure reduces radially from the impact point with depth. Greater pressures are recorded when the measurement location is in front of the centre of the module face, and the distance between the measurement location and the centre of the module face is between 200 and 800 mm in the numerical model and field tests at both 0.7 and 1.1 m depths. Therefore, it can be observed that pressures are non-uniformly distributed under the contact face between the soil and the 3-sided roller due to the curved features of the roller module. This is consistent with a similar conclusion made by Scott et al. (2016) with respect to the 4-sided roller. In general, the numerical model provides reasonable predications of pressures imparted by the 3-sided roller at different depths, and the relationship between peak pressure and offset distance.

Therefore, it can be concluded that numerical results are in good agreement with the field observations in terms of ground settlements and recorded peak pressures, and hence, the numerical model is shown to be able to simulate the behaviour of the 3-sided roller and predict, with an appropriate degree of confidence, ground improvement induced by the roller.

5. Influence of twin modules on ground improvement

As mentioned above, and shown in Fig. 1, unlike the 4-sided roller, both the 3- and 5-sided rollers consist of twin modules which are separated by a distance of approximately 1170 mm. To date, when reporting the soil improvement induced by the 3-sided roller, such as the potential energies reported by Heyns (1998) and Landpac (2020) and the depth of influence presented in Guanbao et al. (2014) and Zhongqing et al. (2019), the total weight of the roller is generally adopted in the calculation. Doubt exists as to the extent to which each of the two separate modules improves the ground. If the total weight of the roller (13-t) is used to calculate the soil improvement, it implies that the effectiveness of twin modules is considered as a single module. Whereas, the distance between the two modules indicates that there is an area of soil that is not compacted, and this is also the reason for the requirement for a second run (straddling pass). Therefore, this section explores the effect, on ground improvement, of the twin modules separated by 1170 mm, and also when there is no separation between the twin modules. This will assist in assessing the effect of the separation distance, but also facilitate direct comparison with the 4-sided roller.

In order to analyse the effects of the twin modules on ground improvement, soil movement obtained from the numerical model is plotted, as shown in Fig. 10. During compaction, soil particles are rearranged, and in some cases fractured, by the applied energy; therefore, the movement of the soil particles is a direct indicator of ground improvement due to the roller. Fig. 10a shows velocity vectors of soil particles when the roller impacts the ground during the first pass. It is clear that there are two zones of soil that are influenced by the two modules, and the shapes of these two zones are similar, except that the soil movement induced by the left module, near the edges of the chamber, is constrained and, hence, soil improvement is compromised. It is clear that soil particles beneath the two modules are significantly compacted, as indicated by the downward velocity vectors. Each of the two modules has its own influence zone, which reveals that the soil beneath one module is not improved by the other, and only the soil particles located near region A (as shown in Fig. 10a) are affected by the compactive energy from both of the modules.

One might argue that these only occur for the first few passes, as the soil is initially at its loosest state, and the compactive energy cannot readily propagate through the soil. To address this, soil velocity vectors during the 15th pass are presented in Fig. 10b. As can be seen, the magnitudes of the velocity vectors are smaller when compared with

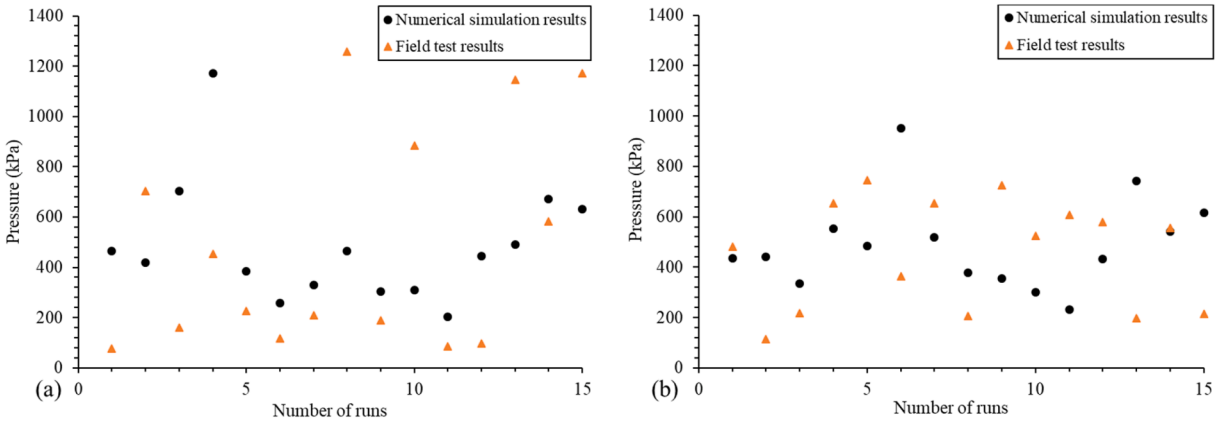

Fig. 7. Pressures measured from odd runs in the numerical model and field tests, at: (a) 0.7 m depth, (b) 1.1 m depth.

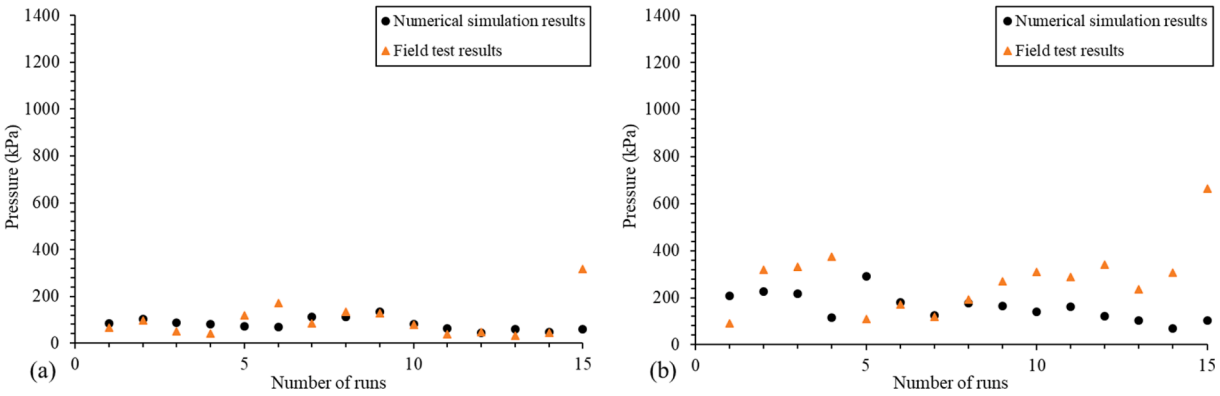

Fig. 8. Pressures measured from even runs in the numerical model and field tests, at: (a) 0.7 m depth, (b) 1.1 m depth.

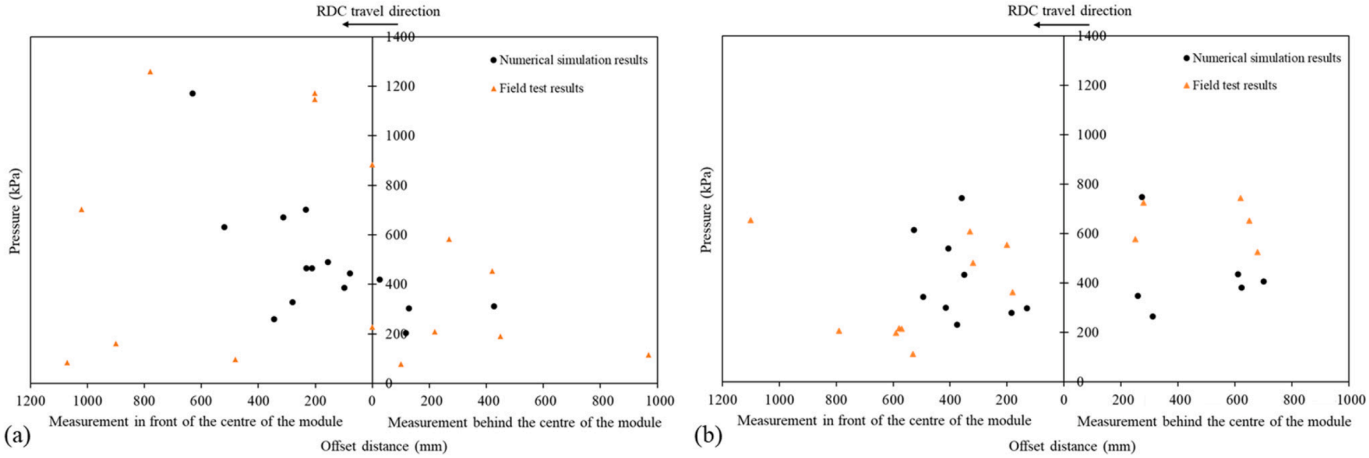

Fig. 9. Peak pressures obtained from numerical simulations and field tests, at: (a) 0.7 m depth, (b) 1.1 m depth.

those of the first pass, since the soil has been compacted and the voids between the particles are reduced; therefore, the soil particles have less ability to move. Although the soil has been densified after 15 passes, it is clear that each module still has its own separate influence zone, and the soil under one module is again not affected by the other. This demonstrates that the soil beneath one module is only compacted by the module above it, and is not improved by the other module and, hence, the twin modules of the 3-sided roller should be treated as two individual modules. In addition, when estimating the soil improvement due to the 3-sided roller (and 5-sided roller, as it has essentially the same design as the 3-sided roller), it is more appropriate to determine the improvement results based on a single module weight rather than the total weight of the roller.

To understand better, the effects of the distance between the twin modules of the 3-sided roller, the 3-sided roller in the numerical model was slightly modified. As shown in Fig. 11, the two modules are joined into a single combined module, with dimensions of 166.7 × 138.5 mm (height × width) and weight of 5.92 kg, which corresponding to a full-size module with dimensions of 2167 × 1800 mm (height × width) and a weight of 13-t. The velocity vectors of soil induced by the impact of the combined module during the first pass are displayed in Fig. 11. It can be seen clearly that the soil directly beneath the module is compacted and moves downwards. Particles located outside this path are pushed to the side. The movement of the soil particles forms an influence zone which is similar to that induced by the separate twin modules shown in Fig. 10. Comparing the effectiveness of the combined module with that of the separate twin modules, the former has a greater depth of influence and it imparts larger energies to the soil, as evidenced by the velocity vectors at deeper depths in Fig. 11. The discrepancy between the ground improvement induced by the combined module and that of the twin modules further confirms that, the ground improvement results such as the energy imparted to the ground and the depth of influence, need to be calculated and reported for each of the twin modules that comprise the 3-sided roller.

6. Energy delivered by the 3-sided roller

As described earlier, compared with traditional (non-dynamic) compaction techniques, RDC is able to improve soil at a greater depth due to the combination of both potential and kinetic energies, which are delivered simultaneously to the soil with each impact. Therefore, in order to investigate the effectiveness of the 3-sided roller, it is essential to assess the imparted energy. In the numerical model, the energy imparted to the ground by a single impact is calculated based on the motion of the roller. The horizontal velocity of the roller is defined in the model according to the speed of the full-size, 3-sided roller adopted in field tests. The vertical speed of the roller is not constrained and is simulated by the model based on the horizontal and rotational speeds, the ground conditions and the characteristics of the undulating surface left by previous roller passes. In addition. The hydraulic accumulator on the full-size, 3-sided roller is modelled as an equivalent spring according to Heyns (1998). By interrogating the energy results from several roller impacts, the energy delivered to the soil is obtained. The energy calculated by the numerical model was upscaled to the prototype scale using Eq. (6). Based on the upscaled energy results, it is concluded, with 95% confidence interval, that the 3-sided roller delivers approximately 22.5 ± 3 kJ per module to the ground with each impact. This value is then

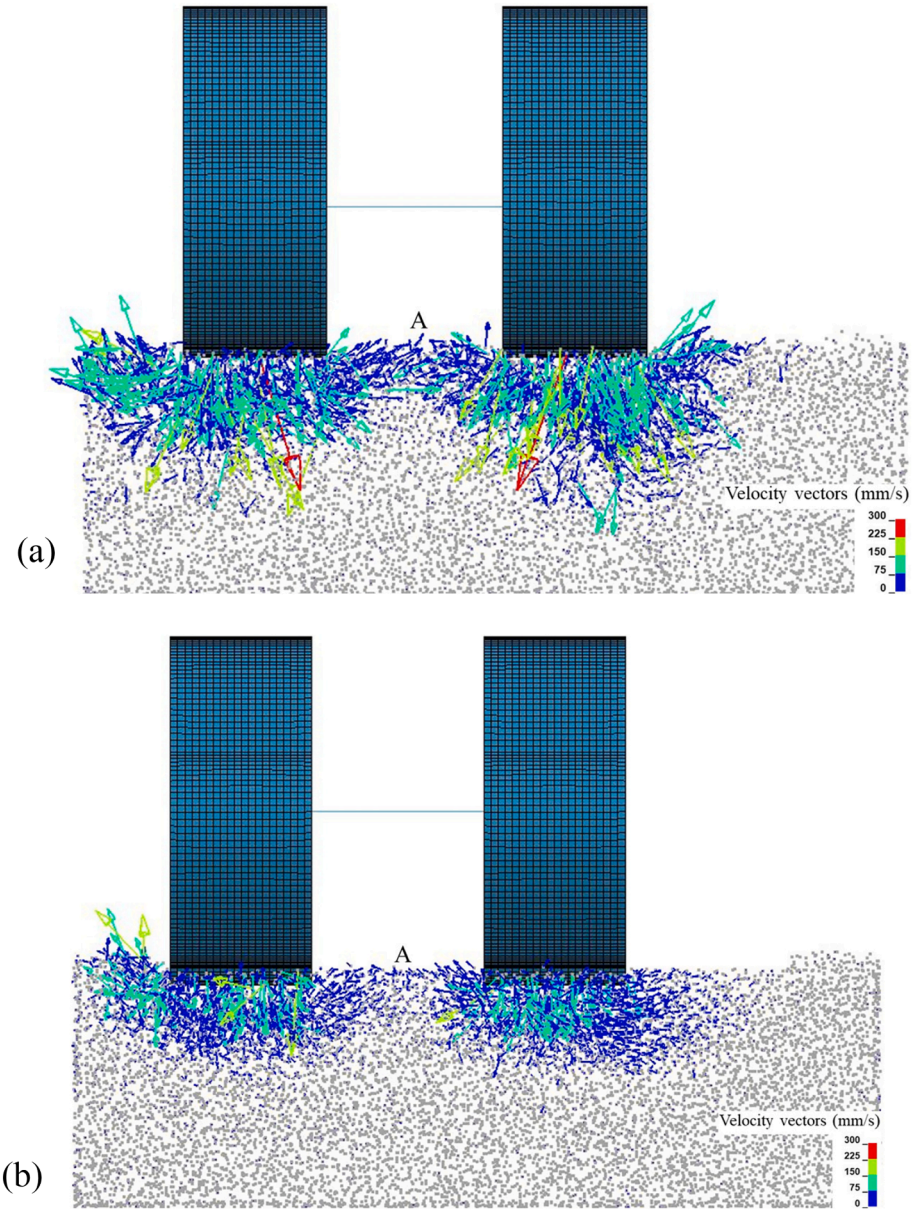

Fig. 10. Velocity vectors of soil particles at the impact of the roller obtained from the numerical model during: (a) the first pass, (b) the 15th pass.

compared with that calculated from relationships proposed by Bradley et al. (2019), as given in Eqs. (7)–(9). In this study, the impact duration is approximately 0.07 s.

$$E_{Roller\_kinetic} = \frac{1}{2} \times M_{Roller} \times \left(v_y{}^2 + v_z{}^2\right) + \frac{1}{2} \times I_{Roller} \times \omega_y{}^2 \tag{7}$$

$$E_{Roller\_potential} = M_{Roller} \times g \times h_{Roller} \tag{8}$$

$$\Delta E = \frac{1}{2} \times M_{Roller} \times \left(v_{yi}{}^2 - v_{yf}{}^2\right) + \frac{1}{2} \times M_{Roller} \times \left(v_{zi}{}^2 - v_{zf}{}^2\right) + \frac{1}{2} \times I_{Roller} \times \left(\omega_{yi}{}^2 - \omega_{yf}{}^2\right) + M_{Roller} \times g \times \Delta h_{Roller} \tag{9}$$

where $E_{Roller\_kinetic}$ is the kinetic energy of the roller; $E_{Roller\_potential}$ is the gravitational potential energy of the roller; ΔE is the energy delivered to the soil at a single impact; M_{Roller} is the mass of the roller; I_{Roller} is the moment of inertia of the roller; h_{Roller} is the height of the roller's centroid above the ground surface; v_y, v_z, and ω_y are the horizontal, vertical, and angular velocities, respectively; v_{yi} and v_{yf} are the horizontal velocities just before and just after the roller impact, respectively; v_{zi} and v_{zf} are the vertical velocities just before and just after the roller impact, respectively; ω_{yi} and ω_{yf} are the angular velocities just before and just after the roller impact, respectively; and Δh_{Roller} is the change in the height of the roller's centroid in the impact duration.

A random roller impact, in the numerical model, is selected to calculate the energy imparted to the soil using Eqs. (7)–(9). The angular velocities just before and just after this impact are 3.41 and 2.83 rad/s, respectively. The horizontal velocity of the roller starts to increase when the roller achieves its highest position and the horizontal velocities just before and just after this impact are 248 and 235 mm/s, respectively, which corresponding to 3.224 and 3.055 m/s for the full-size roller [Eq. (3)]. The vertical velocity of the roller just before this impact is 109 mm/s, which corresponding to 1.417 m/s for the full-size roller. The vertical velocity of the roller just after the impact is zero. The mass moment of inertia of the roller, I_{Roller}, is calculated according to the specification (the radial length to the module's centroid, r and the mass, m) of the Landpac standard 13-t, 3-sided roller, and is found to be 4.788×10^9 kg. mm^2. The change in the height of the roller's centroid in this impact duration is approximately 7 mm, which is then upscaled using Eq. (1) to

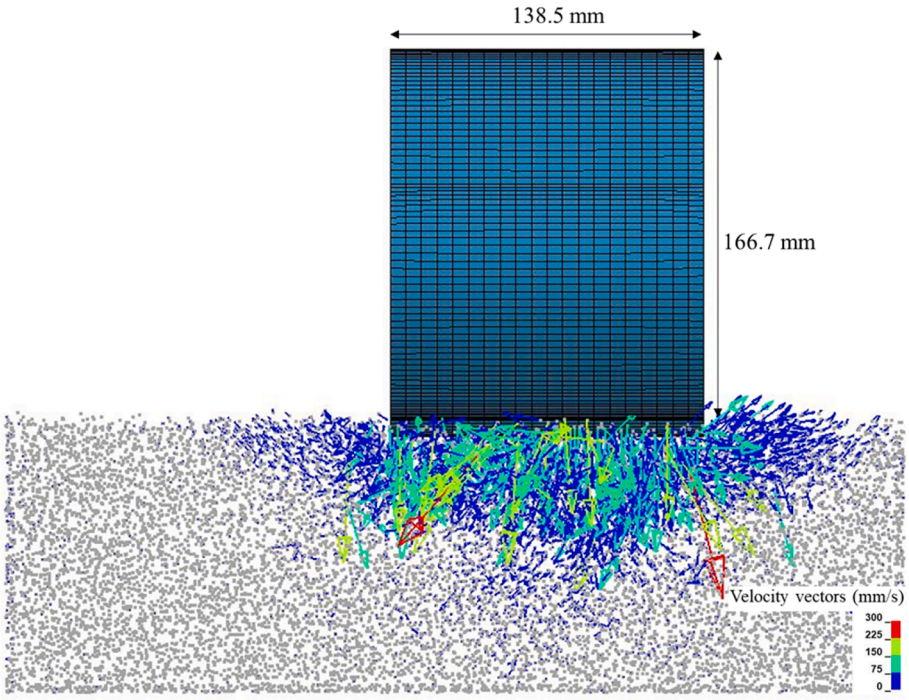

Fig. 11. Velocity vectors of soil particles at the impact of the roller obtained from the modified numerical model during: the first pass.

0.091 m for the full-size roller. By substituting the angular velocities, the upscaled horizontal velocities, M_{Roller}, I_{Roller} and Δh_{Roller} into Eqs. (7)–(9), the energy delivered to the soil at this impact is calculated as approximately 20.1 kJ per module. It can be seen that the energy measured by the numerical model is consistent with that calculated from the energy equation [Eq. (9)]. In addition, from the numerical model, the height differences between the roller's highest location and the location of the roller just after the impact is approximately 17.2 mm, which corresponding to 0.22 m for the full-size roller. The change in potential energy of the roller after it drops from its highest position is then calculated as approximately 14 kJ per module.

Heyns (1998) calculated the energy delivered by the 3-sided roller by undertaking both theoretical and empirical analyses. The author placed an accelerometer on the axle of the roller to measure its motion and also constructed a numerical model based on a mathematical model using the *MATLAB* program. The motion of the roller in the numerical model was validated against that measured by the accelerometer. Heyns (1998) reported that the magnitude of the gravitational potential energy is approximately 23 kJ and the total energy delivered by the 3-sided roller per impact is 17.6 kJ, at approximately 12 km/h. The total energy imparted to the ground reported by Heyns (1998) is questionable as the changes in horizontal and angular velocities of the roller provide additional compactive energy to the ground, as one would expect. The change in potential energy of the standard 13-t, 3-sided roller after it drops from its highest position reported on Landpac (2020) is 25 kJ. The energy delivered to the ground reported by Heyns (1998), Landpac (2020) and predicted by the numerical model are summarised in Table 1. The change in potential energy of the roller after it drops from its highest position predicted by the numerical model is consistent with that from Heyns (1998) and Landpac (2020), since the result predicted by the numerical model (14 kJ) is for each of the twin modules that comprise the 3-sided roller, while Heyns (1998) and Landpac (2020) calculated and reported the change in potential energy of the roller based on the total weight of the roller.

Table 1
Energy of the 3-sided roller.

	Total energy delivered to the ground per impact (kJ)	The change in potential energy of the roller (kJ)
Heyns (1998)	17.6	23
Landpac (2020)	–	25
Numerical model	22.5 ± 3	14

7. Depth of influence

It has been acknowledged by several researchers that, compared with circular drum rollers, RDC is able to improve the soil to a greater depth. The depth to which RDC can improve the density of the ground is an important parameter in quantifying its effectiveness. This depth is known as the *depth of influence* of RDC. In field tests, the depth of influence is often assessed by comparing results of in situ tests (such as, dynamic cone penetrometer testing and cone penetration tests) obtained before and after compaction. However, in field conditions, soil properties vary with depth, which may cause difficulties and problems in the application of these pre- and post-compaction tests and the interpretation of test results. Scott et al. (2019a) proposed Eq. (10) to calculate the depth of influence of the 4-sided roller using an energy-based approach. Applying this equation to the 3-sided roller, with a weight of 6.5-t operated at 11 km/h, the k value is calculated as approximately 1.57, using the energy imparted to the soil (22 kJ) per module divided by the change in gravitational energy (14 kJ) per module (reported in the previous section). An n value of 0.8 is adopted for the Sandy Gravel soil used in this study. Hence, from Eq. (10), the estimated depth of influence for each of the twin modules of the 3-sided roller is approximately 1.5 m. In addition, Scott et al. (2019a) proposed the application of the depth of major improvement (DMI) concept to RDC, which is defined as the depth of soil which is improved to meet a target criterion that can be achieved by conventional compaction equipment in thin lifts. The DMI implies the thickness of the soil layer that can be compacted by RDC. Using Eq. (11), the predicted DMI for the 3-sided roller is between 0.75 and 1 m.

$$D = k\left(n\sqrt{mh}\right) \tag{10}$$

where k is the ratio of the total energy delivered to the ground divided by the change in gravitational potential energy at a single impact; n is an empirical factor which relates to soil conditions (0.3–0.8); m is the mass of the roller module in tonnes; and h is lift height in metres.

$$\mathrm{DMI} = r \bullet D \tag{11}$$

where r is a constant (0.5–0.67).

In order to examine the relationship between the depth of influence, DMI, induced pressures and soil displacements, the maximum recorded pressures over 15 roller passes, and soil displacements measured after 15 passes in the numerical model, are plotted against depth in Fig. 12. To keep consistency with previous sections, the upscaled results are presented in Fig. 12. It can be seen that, both pressures and soil displacements show decreasing trends with respect to increasing depth, as expected, which indicates energy delivered by the roller dissipates with depth. The pressure and soil displacement plots follow similar trends, suggesting that soil displacement is closely related to the imparted pressure. The major difference between the pressure and soil displacement distributions is that the soil displacement is less than 2 mm at 1.4 m depth; however, the peak pressure has a value of approximately 700 kPa at the same depth. The soil displacement trend line suggests that the displacement is close to zero below 1.5 m. In contrast to this, the numerical peak pressure trend line implies that the roller still has influence below 1.5 m depth. These results suggest that the induced pressure at a greater depth does not necessarily result in a meaningful change in soil displacement, or density, since the induced pressure at greater depths may only cause the soil to deform elastically, with no significant plastic deformation upon the removal of pressure as the roller travels away from the region in question. In addition, the pressures presented in Fig. 12a are peak pressures recorded from among the 15 roller passes, and these values cannot be achieved in each pass. From Fig. 12b, it can be observed that the majority of soil displacement occurs within the top 1.1 m, and soil movement is less significant beyond this depth. Based on the results of soil displacement, it is concluded that, the depth of influence and DMI predicted by the numerical model are approximately 1.5 and 1.1 m, respectively.

The depth of influence and DMI of the combined module are also investigated to compare with those calculated from Eqs. (10) and (11). The chamber is slightly modified to reduce the width and is deeper, as suggested by the velocity vectors in Fig. 11. The dimensions of the modified chamber are 600 × 280 × 180 mm (length × width × height). The combined module is again operated up to 15 passes. The maximum pressure recorded during 15 passes, and soil displacements after 15 passes, are plotted against depth in Fig. 13. Since no prototype of the combined module exists in practice, the pressures and displacements presented in Fig. 13 are not upscaled. The peak pressure trend line indicates that the combined module continues to influence the ground below a depth of 155 mm; however, as shown in Fig. 13b, the soil displacement is close to zero below 155 mm. It can also be observed in Fig. 13b that the most significant soil displacements occur above approximately 95 mm depth. Therefore, based on Fig. 13, the depth of influence and DMI of the combined module are approximately 155 and 95 mm, respectively, which equate to 2 and 1.2 m, respectively, at prototype scale [using Eq. (1)]. If the total weight of the 3-sided roller (13-t), is used in Eqs. (10) and (11) to calculate the depth of influence and DMI, instead of 6.5-t, the values are increased to 2.1 and 1.1–1.4 m, respectively. It can be seen that the depth of influence and DMI of the combined module are similar to those calculated from Eqs. (10) and (11), which further supports the conclusion that, when applying proposed equations to calculate depth of influence and DMI of the 3-sided roller, a single module weight, rather than the total weight of the roller should be used, since the soil beneath one of the roller modules is solely improved by the module above it.

8. Summary and conclusions

This paper has developed a combined three-dimensional FEM-DEM model using LS-DYNA to study the performance of the Landpac standard 13-t, 3-sided roller. The FEM is used to describe the characteristics of the roller modules and the DEM is adopted to simulate the behaviour of the soil particles. The numerical model is validated against a field study that was conducted using the same soil and the corresponding full-size, 3-sided roller. Numerical results are compared against field data from two aspects, namely ground settlements and pressures at 0.7 and 1.1 m depths. The numerical results agree well with the field data, which implies that the numerical model is able to predict ground improvement induced by the 3-sided roller, with an acceptable degree of confidence.

The influence of twin modules on ground improvement is examined using the numerical model, and it is found that each module has its own separate influence zone and the soil beneath one module is only compacted by the module above it. Therefore, the current practice of calculating and describing the energy imparted to the ground and the depth of influence using the total weight of the 3-sided roller should be avoided as it overestimates the energy delivered to the ground and the depth of influence.

The validated numerical model is then used to investigate the energy delivered to the ground and the depth of influence. It is concluded that, the energy imparted by each of the twin modules of the 3-sided roller to the underlying soil, when operated at 11 km/h, is approximately 22.5 ±

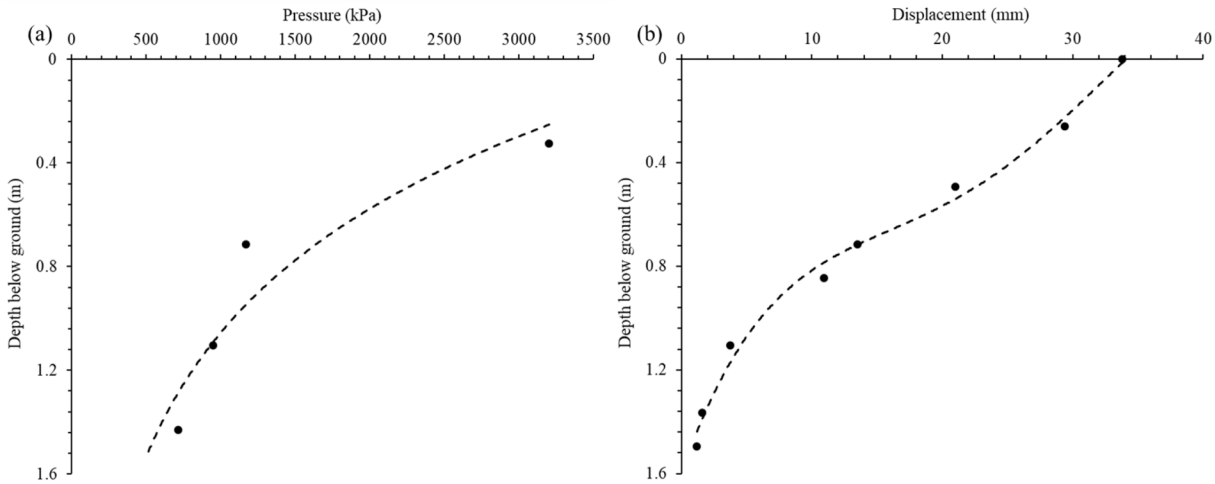

Fig. 12. Pressures and displacements at different depths predicted by the numerical model: (a) peak pressures over 15 passes, (b) soil displacements after 15 passes.

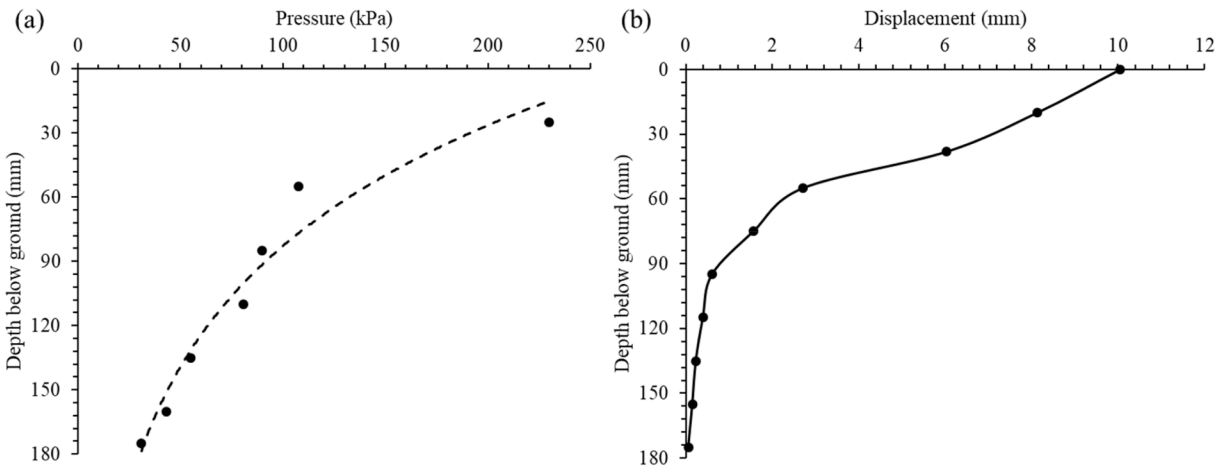

Fig. 13. Pressures and displacements at different depths induced by the combined module: (a) peak pressures over 15 passes, (b) soil displacements after 15 passes.

3 kJ per impact with 95% confidence. The depth of influence is predicted to be approximately 1.5 m for granular soils investigated in this study.

In general, the results of this study provide further insights into the behaviour of the 3-sided roller on granular soils. All of the findings in this study are based on the results of a single operating speed and a single module mass. Future research will explore the influence of operating speed and module mass on the ground improvement derived from the 3-sided roller.

Funding statement

This research did not receive any specific grant from funding agencies in the public, commercial, or not-for-profit sectors.

CRediT authorship contribution statement

Yue Chen: Conceptualization, Methodology, Software, Formal analysis, Writing – original draft. **Mark B. Jaksa:** Conceptualization, Writing – review & editing, Supervision. **Brendan T. Scott:** Conceptualization, Writing – review & editing, Formal analysis. **Yien-Lik Kuo:** Writing – review & editing, Formal analysis.

Declaration of Competing Interest

The authors declare that they have no known competing financial interests or personal relationships that could have appeared to influence the work reported in this paper.

Data availability

Data will be made available on request.

Acknowledgements

The authors wish to acknowledge the computational resources provided by the Phoenix HPC service at the University of Adelaide.

References

Altaee, A., Fellenius, B.H., 1994. Physical modelling in sand. Can. Geotech. J. 31, 420–431.
Avalle, D., Grounds, R., 2004. Improving pavement subgrade with the “square” impact roller. SATC 2004.
Avalle, D.L., Mckenzie, R.W., 2005. Ground improvement of landfill site using the square impact roller. Aust. Geomech. 40, 15–21.
Avalle, D., Carter, J., 2005. Evaluating the improvement from impact rolling on sand. In: Proc. 6th Int. Conf. on Ground Improvement Techniques, Coimbra, Portugal, p. 8.
Bian, X.L., Nan, C.L., Xiao, F.Y., Zhou, Z.G., Wang, Z.Q., 2002. FEM analysis of impaction effect for non-column wheels of compacting roller. Chinese Journal of Mechanical Engineering 10.
Bouazza, A., Avalle, D.L., 2006. Effectiveness of rolling dynamic compaction on an old waste tip. In: ISSMGE 5th International Congress on Environmental Geotechnics, Cardiff, 1.
Bradley, A.C., Jaksa, M.B., Kuo, Y.-L., 2019. Examining the kinematics and energy of the four-sided impact roller. In: Proceedings of the Institution of Civil Engineers - Ground Improvement, 172, pp. 297–304.
Calvetti, F., Viggiani, G., Tamagnini, C., 2003. A numerical investigation of the incremental behaviour of granular soils. Rivista italiana di geotecnica 37, 11–29.
Calvetti, F., Di Prisco, C., Nova, R., 2004. Experimental and numerical analysis of soil–pipe interaction. J. Geotech. Geoenviron. 130, 1292–1299.
Chen, Y., Deng, A., Wang, A., Sun, H., 2018. Performance of screw–shaft pile in sand: Model test and DEM simulation. Comput. Geotech. 104, 118–130.
Chen, Y., Jaksa, M., Kuo, Y., Airey, D., 2021a. Experimental analysis of rolling dynamic compaction using transparent soils and particle image velocimetry. Can. Geotech. J. 59 (2), 254–271.
Chen, Y., Jaksa, M., Kuo, Y., Scott, B., 2021b. Discrete element modelling of the 4-sided impact roller. Comput. Geotech. 137.
Chou, H., Lee, C., Chung, Y., Hsiau, S., 2012. Discrete element modelling and experimental validation for the falling process of dry granular steps. Powder Technol. 231, 122–134.
Chuanli, B.X.N., Fenyang, X., Zhiqiang, Z.Z.W., 2002. Fem analysis of impaction effect for non-column wheels of compacting roller. Chin. J. Mech. Eng. 10.
Chung, O., Scott, B., Jaksa, M., Kuo, Y., Airey, D., 2017. Physical modelling of rolling dynamic compaction. Proceedings of the. In: 19th Int. Conf. on Soil Mechanics and Geotechnical Engineering, Seoul, Korea, Sept. 18–22, pp. 905–908.
Ciantia, M., Arroyo Alvarez De Toledo, M., Calvetti, F., Gens Solé, A., 2015. An approach to enhance efficiency of DEM modelling of soils with crushable grains. Géotechnique 65, 91–110.
Ciantia, M.O., Arroyo, M., Butlanska, J., Gens, A., 2016. DEM modelling of cone penetration tests in a double-porosity crushable granular material. Comput. Geotech. 73, 109–127.
Coetzee, C., 2016. Calibration of the discrete element method and the effect of particle shape. Powder Technol. 297, 50–70.
Cundall, P.A., Strack, O.D., 1979. A discrete numerical model for granular assemblies. Geotechnique 29, 47–65.
Davidson, M.T., Chung, J.H., Teng, H., Han, Z., Le, V., 2015. Volume-averaged stress states for idealized granular materials using unbonded discrete spheres in LS-DYNA®. In: 10th European LS-DYNA Conference, Würzburg, Germany.
Davies, M., Mattes, N., Avalle, D., 2004. Use of the impact roller in site remediation and preparation for heavy duty pavement construction. In: International Geotechnical and Pavements Engineering Conference, 2nd, Melbourne, Victoria, Australia.
Evans, T.M., Valdes, J.R., 2011. The microstructure of particulate mixtures in one-dimensional compression: numerical studies. Granul. Matter 13, 657–669.
Feng, Y., Owen, D., 2014. Discrete element modelling of large scale particle systems—I: Exact scaling laws. Comp. Part. Mech. 1, 159–168.
Gabrieli, F., Cola, S., Calvetti, F., 2009. Use of an up-scaled DEM model for analysing the behaviour of a shallow foundation on a model slope. Geomech. Geoeng. Int. J. 4, 109–122.
Guanbao, Y., Qing, L., Zhongqing, C., Haifei, Q., Sheng, L., 2014. Analysis on impact energy and effective reinforced depth of impact roller compaction. Geotechn. Investig. Survey. 16–19.
Heyns, S., 1998. Response analysis of an impact compactor. In: Report LG198/013, Project No020-DP. Laboratory for Advanced Engineering Pty Ltd., University of Pretoria, Pretoria, South Africa.
Jaksa, M.B., Scott, B.T., Mentha, N., Symons, A., Pointon, S., Wrightson, P., Syamsuddin, E., 2012. Quantifying the zone of influence of the impact roller. In: ISSMGE-TC 211 International Symposium on Ground Improvement IS-GI Brussels.

Kim, K., 2011. Numerical simulation of impact rollers for estimating the influence depth of soil compaction. Texas A & M University.
Kuo, Y., Jaksa, M., Scott, B., Bradley, A., Power, C., Crisp, A., Jiang, J., 2013. Assessing the effectiveness of rolling dynamic compaction. In: Proceedings of the 18th International Conference on Soil Mechanics and Geotechnical Engineering, Paris.
Landpac, 2020. https://www.landpac.com.au/plant (accessed 05/08/2021).
Li, Y., Airey, D., Jaksa, M., 2020. Evaluating the effective depth of rolling dynamic compaction with a three-sided compactor. Int. J. Phys. Modell. Geotech. 0, 1–15.
Lin, H., Suleiman, M.T., Jabbour, H.M., Brown, D.G., 2018. Bio-grouting to enhance axial pull-out response of pervious concrete ground improvement piles. Can. Geotech. J. 55, 119–130.
LSTC, 2018. LS-DYNA Keyword User's Manual. Livermore Software Technology Corporation, Livermore, California. ISBN: 0–9,778,540–2-7.
National Instruments, 2019. http://www.ni.com/en-us/shop/labview.html (accessed 03/05/2022).
Pinard, M., 1999. Innovative developments in compaction technology using high energy impact compactors. In: Proceedings 8th Australia New Zealand Conference on Geomechanics: Consolidating Knowledge, 775. Australian Geomechanics Society.
Rajarathnam, P., Masoudian, M.S., Airey, D.W., Jaksa, M.B., 2016. Model tests of rolling dynamic compaction. In: Proc. 19th Southeast Asian Geotechnical Conf. and 2nd AGSSEA Conf. Kuala Lumpur Malaysia.
Ranasinghe, R., Jaksa, M., Kuo, Y., Nejad, F.P., 2017a. Application of artificial neural networks for predicting the impact of rolling dynamic compaction using dynamic cone penetrometer test results. J. Rock Mech. Geotech. Eng. 9, 340–349.
Ranasinghe, R.A.T.M., Jaksa, M.B., Pooya Nejad, F., Kuo, Y.L., 2017b. Predicting the effectiveness of rolling dynamic compaction using genetic programming. In: Proceedings of the Institution of Civil Engineers-Ground Improvement, 170, pp. 193–207.
Ranasinghe, R., Jaksa, M., Nejad, F.P., Kuo, Y., 2019. Prediction of the effectiveness of rolling dynamic compaction using artificial neural networks and cone penetration test data. Yanshilixue Yu Gongcheng Xuebao/Chinese Journal of Rock Mechanics and Engineering 38, 153–170.
Ranjan, G., Rao, A., 2007. Basic and applied soil mechanics. New Age International.
Scott, B.T., Jaksa, M.B., 2015. A field based study of the effec tiveness of rolling dynamic compaction. In: Ground Improvement Case Histories: Compaction, Grouting and Geosynthetics, Ed. Indraratna, Chu & Rujikiatkamjorn, pp. 429–452.
Scott, B., Jaksa, M., Syamsuddin, E., 2016. Verification of an impact rolling compaction trial using various in situ testing methods. In: Proc. of 5th Int. Conf. on Geotechnical and Geophysical Site Characterisation.
Scott, B., Jaksa, M., Mitchell, P., 2019a. Depth of influence of rolling dynamic compaction. In: Proceedings of the Institution of Civil Engineers-Ground Improvement, pp. 1–10.
Scott, B., Jaksa, M., Mitchell, P., 2019b. Ground response to rolling dynamic compaction. Géotechn. Lett. 9, 99–105.
Scott, B.T., Jaksa, M.B., Mitchell, P.W., 2020. Influence of towing speed on effectiveness of rolling dynamic compaction. J. Rock Mech. Geotech. Eng. 12, 126–134.
Wang, C., Deng, A., Taheri, A., 2018. Three-dimensional discrete element modelling of direct shear test for granular rubber–sand. Comput. Geotech. 97, 204–216.
Zhang, N., Arroyo, M., Ciantia, M.O., Gens, A., Butlanska, J., 2019. Standard penetration testing in a virtual calibration chamber. Comput. Geotech. 111, 277–289.
Zheng, G., Cui, T., Cheng, X., Diao, Y., Zhang, T., Sun, J., Ge, L., 2017. Study of the collapse mechanism of shield tunnels due to the failure of segments in sandy ground. Eng. Fail. Anal. 79, 464–490.
Zheng, G., Tong, J., Zhang, T., Wang, R., Fan, Q., Sun, J., Diao, Y., 2020. Experimental study on surface settlements induced by sequential excavation of two parallel tunnels in drained granular soil. Tunn. Undergr. Space Technol. 98 (103), 347.
Zhongqing, C., Wenliang, L., Man, H., Ogechi Aduramomi, N., Hongbo, C., 2019. On prediction of effective improvement depth of rolling dynamic compaction on shallow ground. J. Shaoxing Univ. 39, 1–6.